Geomorphology 231 (2015) 314–330

Contents lists available at ScienceDirect

Geomorphology

journal homepage: www.elsevier.com/locate/geomorph

Landslide deformation monitoring with ALOS/PALSAR imagery: A D-InSAR geomorphological interpretation method

Romy Schlögel *, Cécile Doubre, Jean-Philippe Malet, Frédéric Masson

Institut de Physique du Globe de Strasbourg, CNRS UMR 7516, Université de Strasbourg/EOST, 5 rue Descartes, 67084 Strasbourg, Cedex, France

ARTICLE INFO

Article history:
Received 31 May 2014
Received in revised form 7 November 2014
Accepted 21 November 2014
Available online 19 December 2014

Keywords:
Landslide
InSAR
ALOS/PALSAR
Displacement monitoring

ABSTRACT

The objective of this work is to propose a geomorphologically-guided method for the interpretation of L-band ALOS/PALSAR interferograms created by Differential Interferometric Synthetic Aperture Radar (D-InSAR). The interferograms are used to estimate the deformation pattern of two rapid and large landslides (Poche, La Valette; South East France). The wrapped and unwrapped phase values are interpreted for different movement types (rotational, translational, and complex sliding) and two ranges of surface displacement rates. Kinematic subunits are detected for both landslides, and zones affected by enlargement or retrogression are identified. The InSAR-derived displacement rates are consistent with ground-based measurements and with remote estimates of the displacement from C-band and X-band satellite SAR sensors. The results demonstrate the potential of L-band ALOS/PALSAR imagery for the monitoring of active landslides with important changes in the soil surface state and covered by vegetation.

1. Introduction

Landslides are one of the most significant geohazards in terms of socio-economic costs, threatening infrastructures and human settlements. The monitoring of their surface displacement is thus crucial for the prevention and forecast of landslides. In regions where large landslides ($>10^5$ m^3) cannot be stabilized and may accelerate suddenly, remote monitoring is often the only solution for surveying and/or early-warning. Techniques using high resolution (HR) to very-high resolution (VHR) space-borne optical and radar (SAR) images provide valuable information to investigate landslide kinematics measuring 1D Line-of-Sight (LoS) and 2D horizontal surface displacements (Delacourt et al., 2007). For instance, digital image correlation (DIC) of VHR optical satellite images has been used to estimate the horizontal component of the displacement with a centimetric accuracy (Booth et al., 2013; Stumpf et al., 2014). To yield a sub-pixel accuracy, adequate image orientation, co-registration, georeferencing and modelling of topographic distortions are of primary importance (Stumpf et al., 2014). In complement to optical images, SAR images have become a widely used source of information for measuring the topography and deformation of the Earth surface. SAR images can be used at regional scales, for basin subsidence or plate tectonics motion monitoring, and local scales, for fault, slope movement or glacier monitoring (Massonnet and Feigl, 1998). Advanced processing of SAR images has proven its ability for landslide detection and mapping (Farina et al., 2006; Cascini et al., 2009; Guzzetti et al., 2012), process monitoring (Hilley et al., 2004; Zhao et al., 2012; Raucoules et al., 2013), hazard assessment (Zhao et al., 2013; Nikolaeva et al., 2014) and risk management (Bardi et al., 2014). The choice of an optimal SAR processing technique depends on several constraints: landslide type (Dikau et al., 1996), range of expected velocity and direction of the displacement (Cruden and Varnes, 1996), areal extension of the moving mass, and land cover (e.g. presence of bare rocks, soils or dense vegetation; Jebur et al., 2014), requested accuracy, and existing catalogue of SAR data (Tofani et al., 2013). Traditional two-pass differential InSAR technique (D-InSAR) has been applied for the monitoring of slow-moving landslides on the order of cm year^{-1} (Catani et al., 2005), whereas persistent scatterers SAR interferometry (PS-InSAR; Ferretti et al., 2001; Hooper, 2004) and small baseline subset (SBAS; Berardino et al., 2002; Tolomei et al., 2013) techniques allow the monitoring of extremely slow-moving landslides on the order of mm year^{-1} (Hilley et al., 2004; Guzzetti et al., 2009). Finally, correlation of SAR amplitude images allows the monitoring of rapid landslides (on the order of m year^{-1}; Raucoules et al., 2013). As each of these techniques has its advantages and limitations, the combination of various SAR/InSAR processing techniques offers new perspectives to investigate variable displacement rates (Lauknes et al., 2010).

In this work, we focus on the analysis of two large landslides characterized by slow to moderate velocity in the order of cm day^{-1} (Cruden and Varnes, 1996). These landslides show a complex spatial pattern of displacement which is challenging to monitor with SAR images because of significant changes in the local morphology, the soil surface state and the vegetation inducing changes of the ground scattering properties between two consecutive image acquisitions. Further, the available SAR archive on these landslides is limited to ascending orbits, thus preventing a complete analysis of landslide movement over all the

* Corresponding author. Tel.: +33 3 68850036; fax: +33 3 68850125.
E-mail address: romy.schlogel@unistra.fr (R. Schlögel).

http://dx.doi.org/10.1016/j.geomorph.2014.11.031
0169-555X/

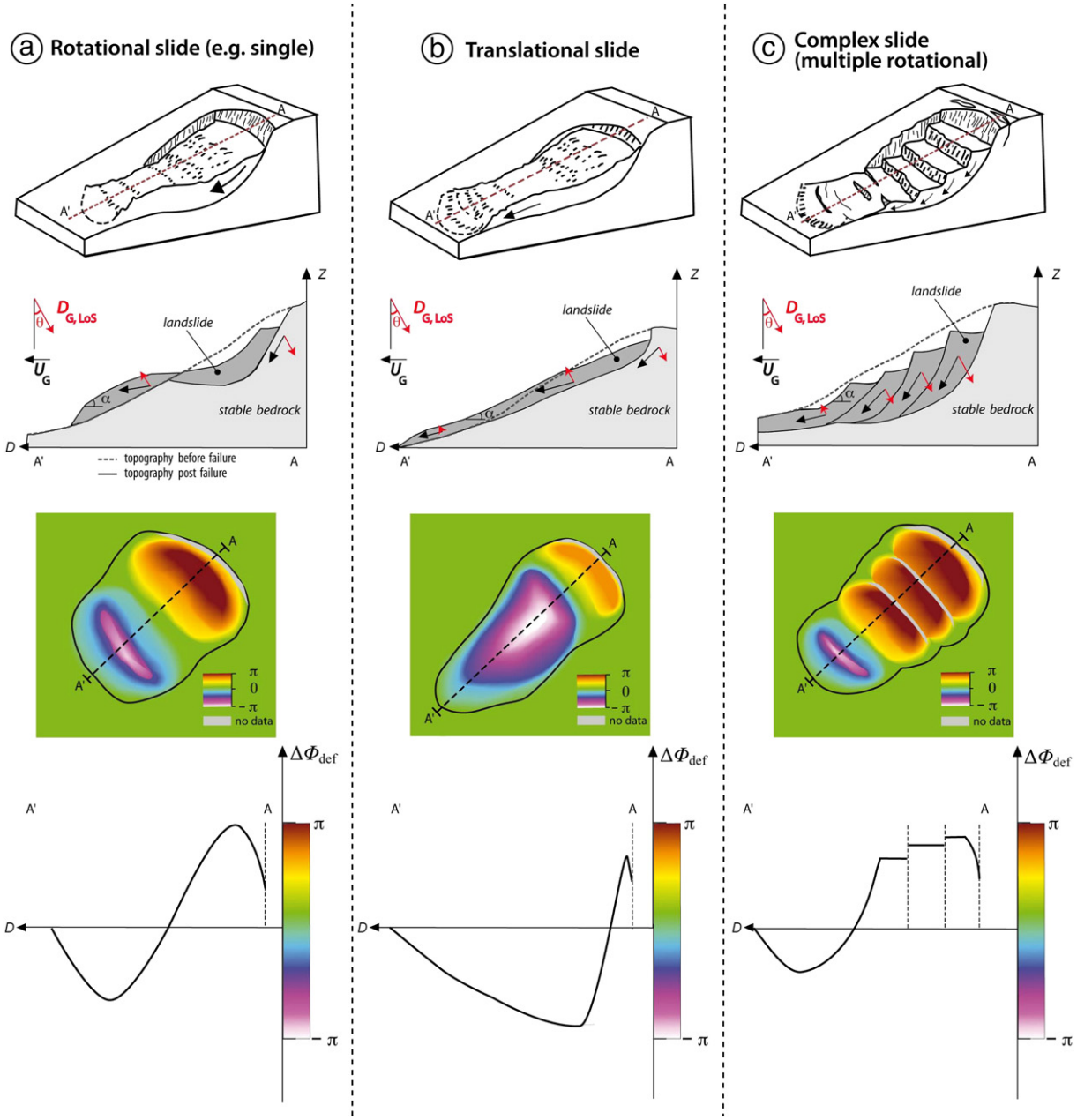

Fig. 1. Displacement pattern, morpho-structures and associated interferometric phase for three landslide types. (a) Rotational slide with a single circular slip surface; (b) translational slide with a nearly planar slip surface parallel to the slope topography; and (c) complex slide with a series of embedded circular slip surfaces. From top to bottom: Three-dimensional view with a longitudinal cross-section of the slope morphology; synthetic spatial distribution of InSAR phase values; and along a longitudinal cross-section. The distribution of phase values (Φ) is based on the following assumptions: (i) the SAR Line-of-Sight (LoS) and the landslide displacement directions are in the same vertical plane, (ii) the slope angle α is smaller than the SAR look angle θ (which is equivalent to a local incidence angle smaller than θ), and (iii) the amplitude of the displacements is small enough to produce a phase variations in the interval $[-\pi, \pi]$. D: horizontal distance along the cross-section profile, Z: elevation; $D_{G,LoS}$: displacement vector along the LoS direction, U_G: displacement vector at the ground. $\Delta\Phi_{def}$: variation of phase values.

affected slope orientations and a measurement of the displacements along the three components (Nikolaeva et al., 2014).

Therefore, we propose a geomorphologically-guided InSAR interpretation method in order to overcome some of the above mentioned constraints of the SAR images and the InSAR technique. The method, developed for L-band ALOS/PALSAR images, is based on the analysis of the spatial distribution of both surface geomorphological features and SAR phase values (Fig. 1). We assume that the direction of the landslide

Table 1
Reference case studies, defined in terms of displacement rate (v) and movement type (m), used to test the applicability of the interpretation method.

	v	m	Landslide type and morphological unit
Case 1	<0.4 cm day^{-1}	Mainly vertical	Rotational slide, ablation zone (Poche landslide)
Case 2	<0.4 cm day^{-1}	Mainly along slope	Translational slide, accumulation zone (Poche landslide)
Case 3	>0.4 cm day^{-1}	Mainly along slope	Translational slide, accumulation zone (La Valette landslide)
Case 4	>0.4 cm day^{-1}	Mainly vertical	Complex slide, ablation zone (La Valette landslide)

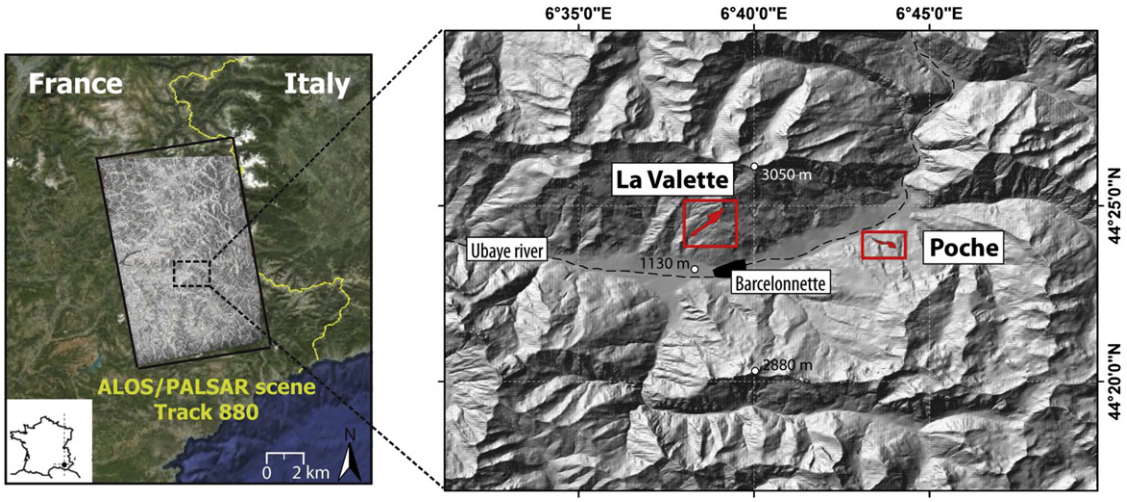

Fig. 2. Location and characteristics of the Poche and La Valette landslides in the Ubaye Valley (South East France) and extension of ALOS/PALSAR SAR scenes.

movement is controlled at depth by the geometry of the slip surfaces, and laterally by the geometry of the stable bedrock slopes confining the landslide mass (Okada, 1985; Muller and Martel, 2000; Petley et al., 2002). The geometry and spatial distribution of discontinuities, such as scarps and grabens upslope, sets of strike-slip and normal fissures on the lateral sides, and compression lobes downslope, are used to infer the movement direction (Travelletti et al., 2012; Stumpf et al., 2013). Large landslides are characterized by rotational, translational or complex style of movement (Fig. 1). Single rotational slides are confined by a circular basal slip surface and are affected by retrogression upslope (Fig. 1a). Translational slides are confined by planar basal slip surfaces and show a surface movement mainly parallel to the hillslope (Fig. 1b). Most landslides are complex and thus involve a combination of rotational and translational movement features with multiple small circular slip surfaces (Fig. 1c).

Fig. 1 also depicts the synthetic spatial distribution of interferometric phase values for these three types of movement. In the landslide upper parts (ablation zone), the vertical displacements (subsidence) are larger than the horizontal (downslope) displacements; this kinematic pattern is represented by positive phase values in the interferograms corresponding to a motion away from the satellite. In the landslide lower parts, vertical displacements (e.g. accumulation) are, most of the time, smaller than horizontal (downhill) displacements; this kinematic pattern is represented by negative phase values in the interferograms corresponding to a motion towards the satellite. Fig. 1 also presents theoretical profiles of the slope topography and of the InSAR phase values for rotational, translational and complex slides. The shape of the phase along the profile, is further used to analyse the direction and amplitude of the movement.

The method is tested on four case studies defined in terms of average landslide displacement rate and style of movement (Table 1). The four case studies represent typical motion and sliding mechanisms observed in the ablation and accumulation zones of the Poche and La Valette landslides (South French Alps, Fig. 2). After presenting the study areas and the InSAR processing technique, we analyse the InSAR data to estimate the displacement field and compare it to *in-situ* displacement measurements. Finally, we focus on the time evolution of the displacement field to analyse the non-steady state behaviour of the landslides.

2. Study areas

The Poche and La Valette landslides are located in the Ubaye Valley (South East France; Fig. 2) and have developed in clay-shale material (Callovo–Oxfordian black marls). The dynamics of these two landslides corresponds to a complex slide with various motion patterns in the ablation and accumulation zones. At first order, the kinematics is controlled by the local geometry of the bedrock and the presence of faults (Le Mignon and Cojean, 2002; Travelletti et al., 2013). The geomorphological characteristics of the landslides are detailed in Fig. 2 and Table 2.

2.1. Poche landslide: geology and kinematics

The Poche landslide is located on the north-facing slope of the Ubaye Valley, 5 km to the East of the town of Barcelonnette (Figs. 2 and 3). The triggering date is not precisely known, but is estimated in the middle of the 19th century. Currently, the landslide extends over a length of 1200 m along the EW to NW direction, and a width of 100 and 300 m in the lower and upper parts, respectively. The maximum landslide depth, estimated by seismic tomography and geotechnical boreholes, ranges from 10 to 25 m (Schmutz, 2000). The mean slope angle is ~15° in the ablation zone and ~20° in the accumulation zone. The volume of the landslide is estimated at ca. 5.0×10^5 m^3 (Schmutz, 2000; Malet and Maquaire, 2003).

For the period 1993–2013, the displacement rates measured by total station on 10 benchmarks are ~1 cm day^{-1} (Malet and Maquaire, 2003). Higher displacement rates, up to 8 cm day^{-1}, have been observed in Spring 2001 and 2008.

The landslide ablation zone consists of a combination of structural rock block slides to the South-East and a large rotational slide to the North-East (Fig. 3a; case 1). The 20°-dipping main scarp limits the

Table 2
Characteristics of the Poche and La Valette landslides in the Ubaye Valley (South East France).

	Location	Triggering date	Elevation (m)	Dimension (L, l; m)	Slope angle (α; °)	Slope direction (β; °)	Lithology
Poche	N Ubaye	>1855	1200–1500	L: 1200; l: 150–300	20 (scarp)–11 (tongue)	305 (scarp)–270 (tongue)	Black marls, moraine
La Valette	S Ubaye	1982	1240–2070	L: 2000; l: 200–500	35 (scarp)–20 (tongue)	230 (scarp)–230 (tongue)	Black marls, limestone, moraine

L: length; l: width.

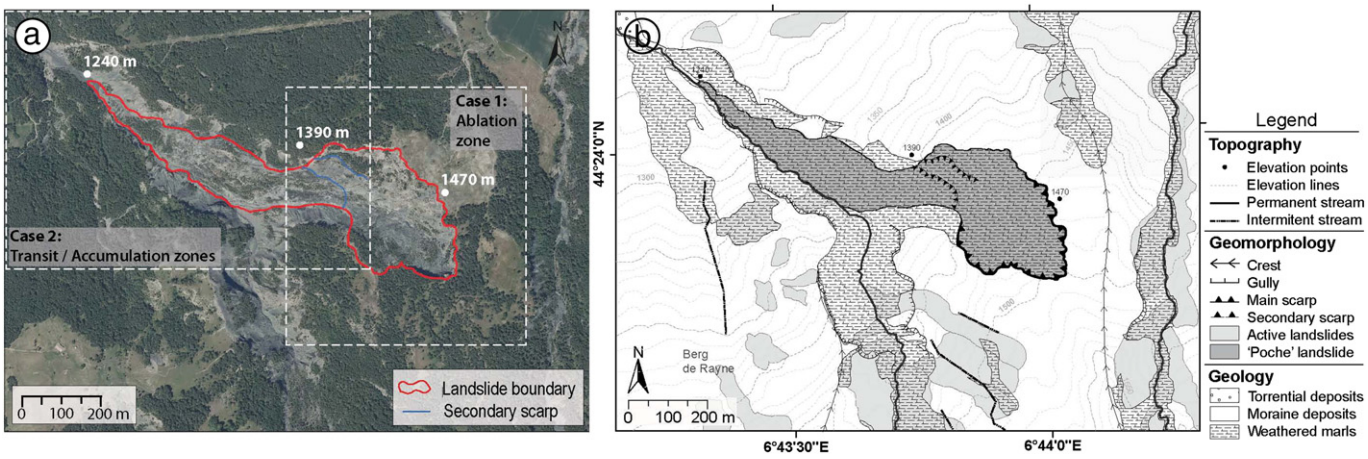

Fig. 3. Morphology of the Poche landslide. (a) Orthophotograph of the landslide in 2009 and location of ablation (case 1) and transit-accumulation zones (case 2); (b) morpho-structural map of the landslide.

~10-m-thick moraine deposits and the Callovo–Oxfordian black marls (Le Mignon and Cojean, 2002). The morphology of the ablation zone is very bumpy with the presence of numerous blocks of marls, secondary scarps and counterslopes.

The transit and accumulation zones present a flow-type morphology with the progressive burial of the thalweg of the Poche torrent (Fig. 3a, case 2). The slope angle of the accumulation zone is, at first order, constant but locally presents a series of small secondary scarps and lobes where ponds are located. The displacement pattern of this zone can be considered as translational.

2.2. La Valette landslide: geology and kinematics

The La Valette landslide is located on the south-facing slope of the Ubaye Valley to the NW of the town of Barcelonnette (Fig. 4a). The landslide, triggered in March 1982, currently extends over a length of

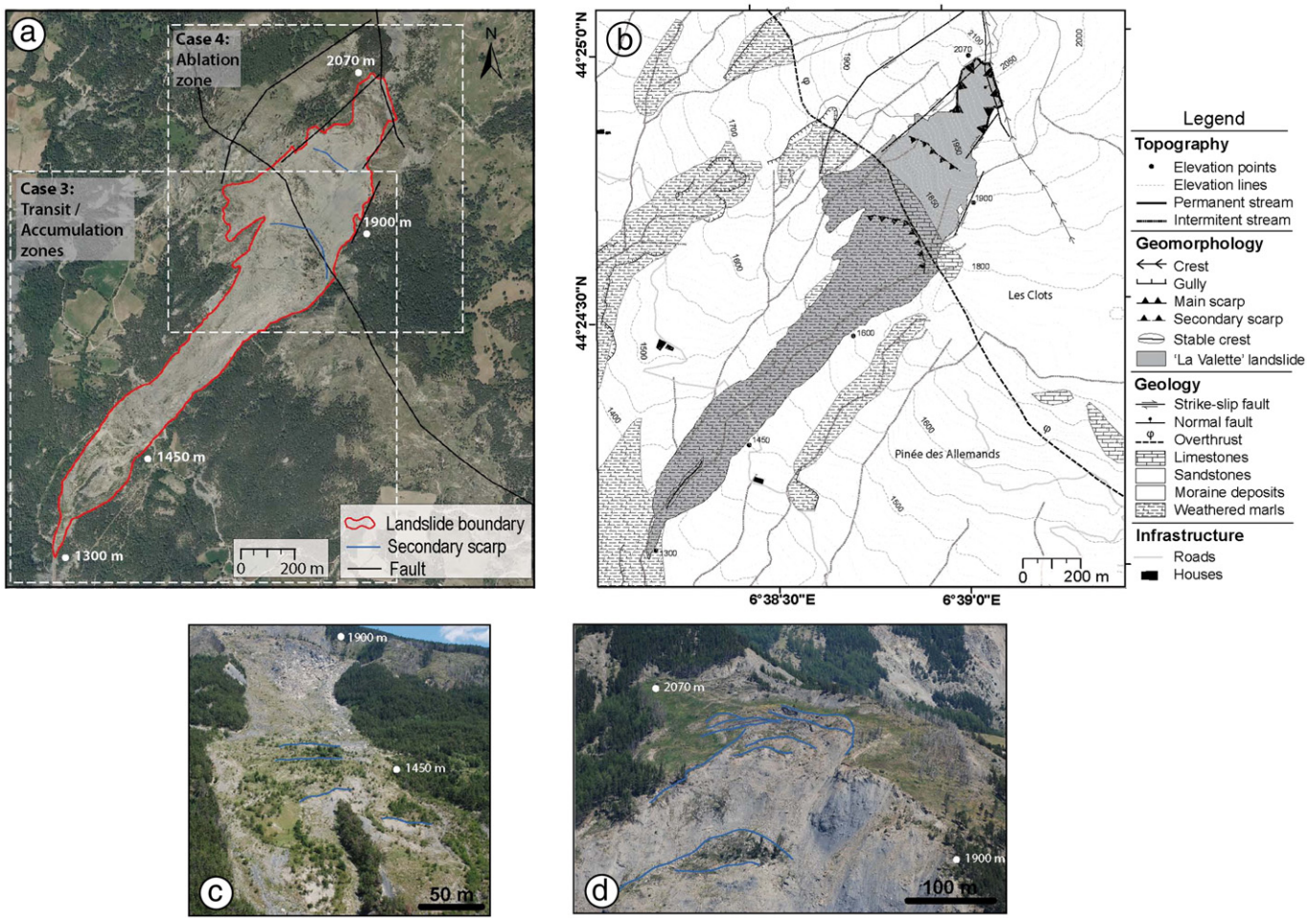

Fig. 4. Morphology of the La Valette landslide. (a) Orthophotograph of the landslide in 2009 and location of ablation (case 4) and transit-accumulation zones (case 3), (b) morpho-structural map of the landslide. (c) Photograph of the transit and accumulation zones in 2009. (d) Photograph of the ablation zone in 2009 including numerous secondary scarps.

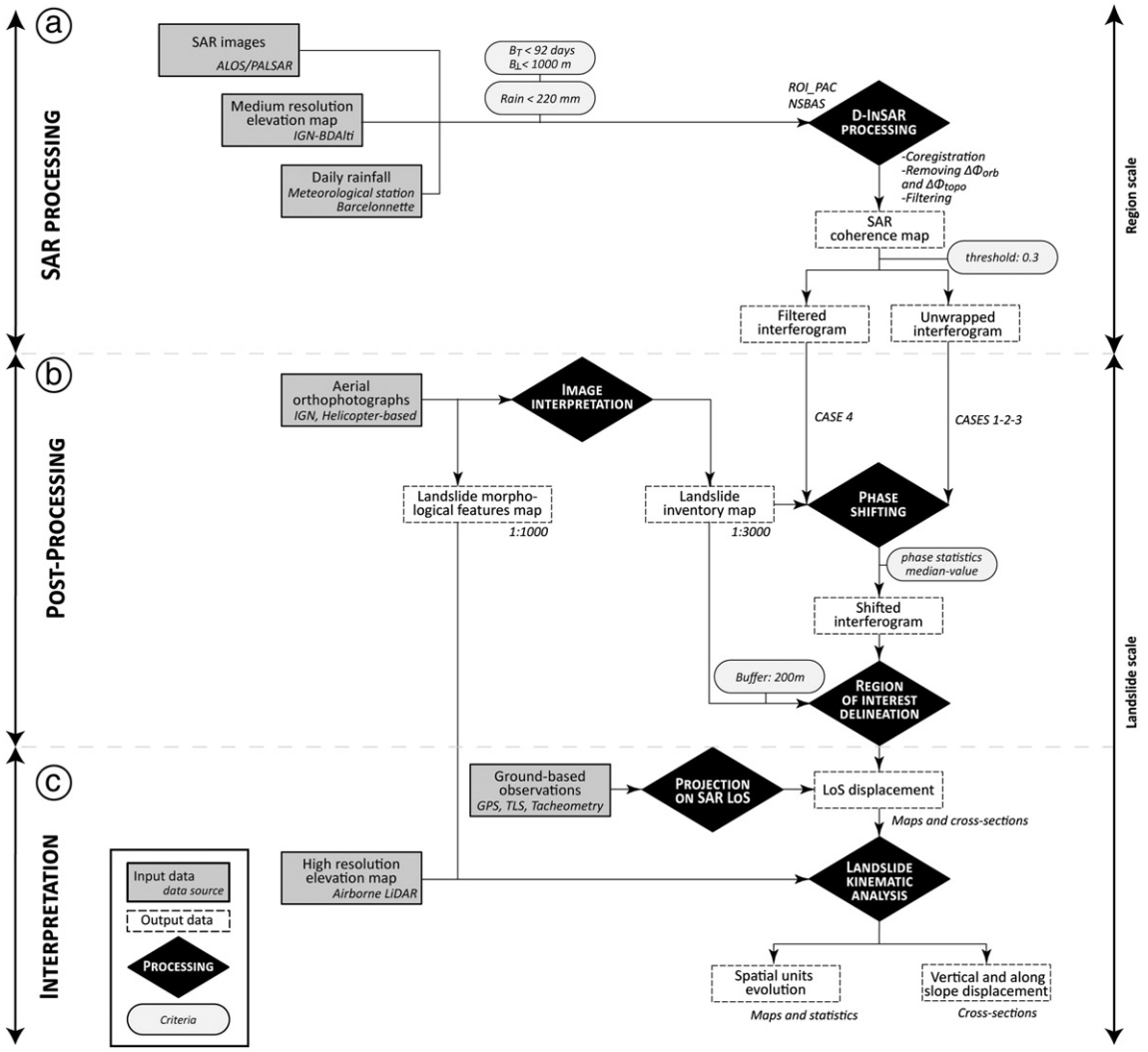

Fig. 5. Methodological flowchart and indications of the data and outputs used at each processing step. (a) SAR images selection and processing. (b) Interferograms post-processing. (c) Interferograms interpretation. The detailed characteristics of the data are presented in Table 3 and Fig. 6.

2000 m along the SW direction. It features a variable width ranging from 200 m in the transit and accumulation zones and 500 m in the ablation zone. The maximum depth, estimated by seismic and electrical resistivity tomography and geotechnical boreholes, ranges from 25 to 35 m (Travelletti et al., 2009; Hibert et al., 2012). The mean slope angle is ~30° at the main scarp and ~20° within the transit zone. The volume of the landslide is estimated at 3.5×10^6 m^3 (Le Mignon and Cojean, 2002). The landslide is located at an overthrust contact between the Callovo–Oxfordian black marls at the base and the Pelat nappe at the top (Turonian and Paleocene flysch and limestone; Fig. 4b; Travelletti et al., 2013).

The displacements are monitored with topometric benchmarks since 1991 (Squarzoni et al., 2005), differential dual-frequency GNSS (Malet et al., 2002; Malet et al., submitted for publication) and an extensometer since 2008. At regular time intervals, displacement maps are also calculated from correlation of optical satellite images (Leprince et al., 2008), satellite radar interferometry (Vietmeier et al., 1999; Squarzoni et al., 2003) and airborne and ground based laser scans (Travelletti et al., 2013). For both periods 1995–1999 and 1999–2003, the displacement rates measured from the correlation of orthophotographs are in the range of 2.5 m yr^{-1} in the accumulation zone and 20 m yr^{-1} in the ablation zone (Delacourt et al., 2007). For the period 1991–1999, Squarzoni et al. (2003) determined from the analysis of ERS-1/2 (C-band) interferograms and four kinematic subunits identified two movement types: a translational sliding with the development of a flow tongue in the transit and accumulation zones (Fig. 4c) and multiple rotational sliding with a slump type morphology in the ablation zone (Fig. 4d).

Table 3
Characteristics of the dataset used for the analysis.

	Poche	La Valette
Topographic data	2007: BD ALTI® Elevation DSM (25 m) 2007: Airborne LiDAR DSM (0.5 m)	2007: BD ALTI® Elevation DSM (25 m) 2007: Airborne LiDAR DSM (0.5 m) 2009: Airborne LiDAR DSM (0.5 m)
Orthophotograph	2007 (0.5 m), 2009 (0.5 m)	2007 (0.2 m), 2009 (0.2 m)
Ground-based displacement data	Total station campaigns on benchmarks (2007–2010)	GNSS campaigns on benchmarks (2008–2010), Permanent GNSS (>2009)

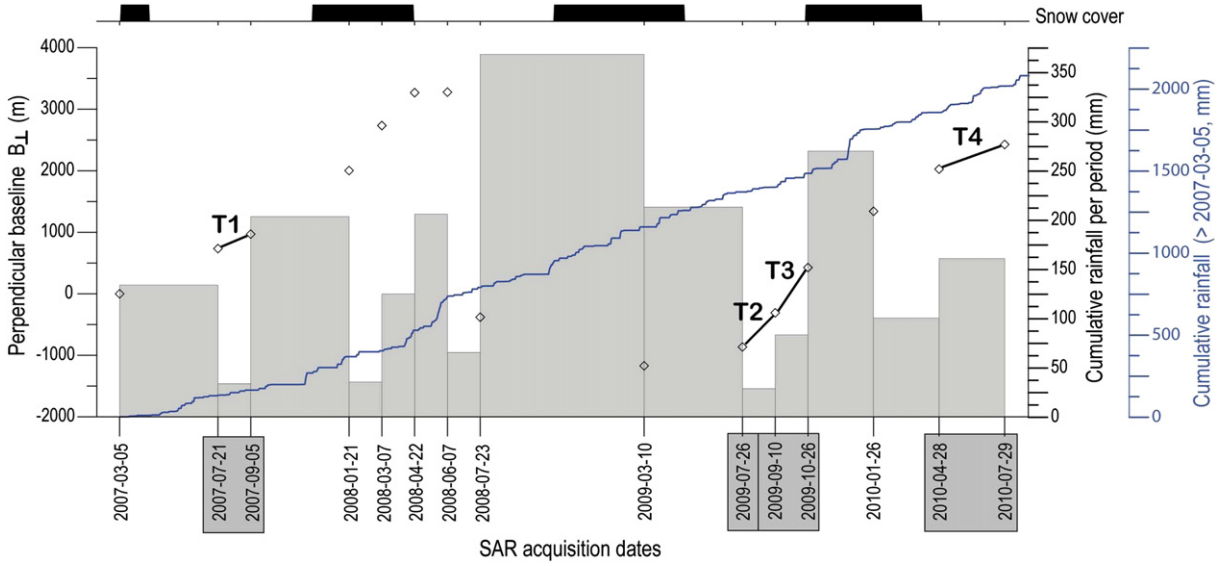

Fig. 6. Time acquisition and perpendicular baseline (white point) of the SAR images together with the cumulative net rainfall between consecutive SAR acquisitions (grey box) and for the complete time period (blue line) at the Barcelonnette meteorological station. The presence of snow cover (black box) is estimated from satellite image analysis. The interferograms T1, T2, T3 and T4, analysed in this work, are indicated.

3. Methodology

The processing and interpretation methodology is summarised in Fig. 5. It includes the selection and processing of SAR images (Fig. 5a), the post-processing of interferograms (Fig. 5b) and the calculation and interpretation of displacement (Fig. 5c). The detailed characteristics of the data are presented in Table 3 and Fig. 6.

3.1. SAR processing

An interferogram consists of the calculation of phase differences ($\Delta\Phi_{int}$) between two co-registered SAR images:

$$\Delta\Phi_{int} = \Phi(t_0) - \Phi(t_1) = \Delta\Phi_{def} + \Delta\Phi_{orb} + \Delta\Phi_{topo} + \Delta\Phi_{atm} + \Delta\Phi_{noise} \quad (1)$$

where $\Delta\Phi_{int}$ is the SAR interferometric phase, $\Delta\Phi(t_0)$ and $\Delta\Phi(t_1)$ are the SAR phase values at respectively day t_0 (reference) and day t_1, $\Delta\Phi_{def}$ is ground deformation (between two acquisition times), $\Delta\Phi_{orb}$ is orbital contribution (due to changes of the satellite orbital geometry), $\Delta\Phi_{topo}$ is topographic contribution, $\Delta\Phi_{atm}$ is atmospheric contribution (due to difference of signal propagation in the atmosphere) and $\Delta\Phi_{noise}$ is noise contribution (corresponding to changes in the scattering properties of the ground surface, changes in the thermal properties of the atmosphere or ground surface, or inaccurate image co-registration; Massonnet and Feigl, 1998).

The SAR data are coregistered using the NSBAS tools (Doin et al., 2011). The interferograms are processed using the ROI-PAC software (Fig. 6a; Rosen et al., 2004). The orbital contribution is corrected with precise satellite orbit data (<1 m) provided by the Japan Aerospace Exploration Agency (JAXA) fitted with a 2D linear offset ramp. The topographic contribution is corrected using the BDALTI® DSM (25 m) resampled at 10 m. with a bilinear interpolation. The topography-correlated phase signal due to the stratified troposphere is removed over the complete SAR scene using the wrapped phase (Beauducel and Briole, 2000;, Doin et al., 2009)

After filtering, we further interpret only the interferograms with coherence values higher than 0.30 (Fig. 5a). Two strategies are used for the interpretation. For cases 1, 2 and 3 (Table 1), the phase values are

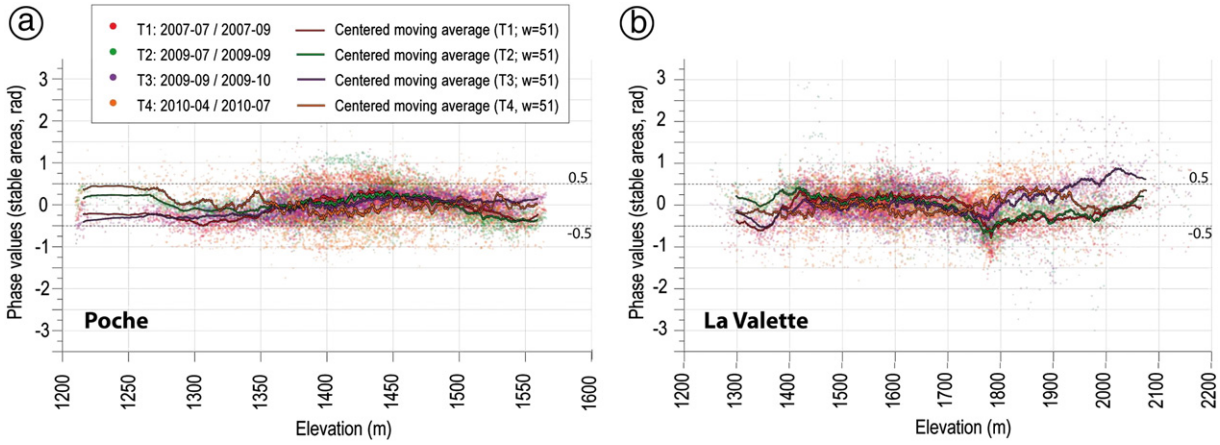

Fig. 7. Variability of phase values with elevation. (a) Phase values for the Poche landslide with respectively 83%, 85%, 96% and 64% of values in the range ±0.5 rad for the periods T1, T2, T3 and T4. (b) Phase values for the La Valette landslide with respectively 76%, 81%, 80% and 72% of values in the range ±0.5 rad for the periods T1, T2, T3 and T4. The centred moving average is calculated for each period with a season w = 51.

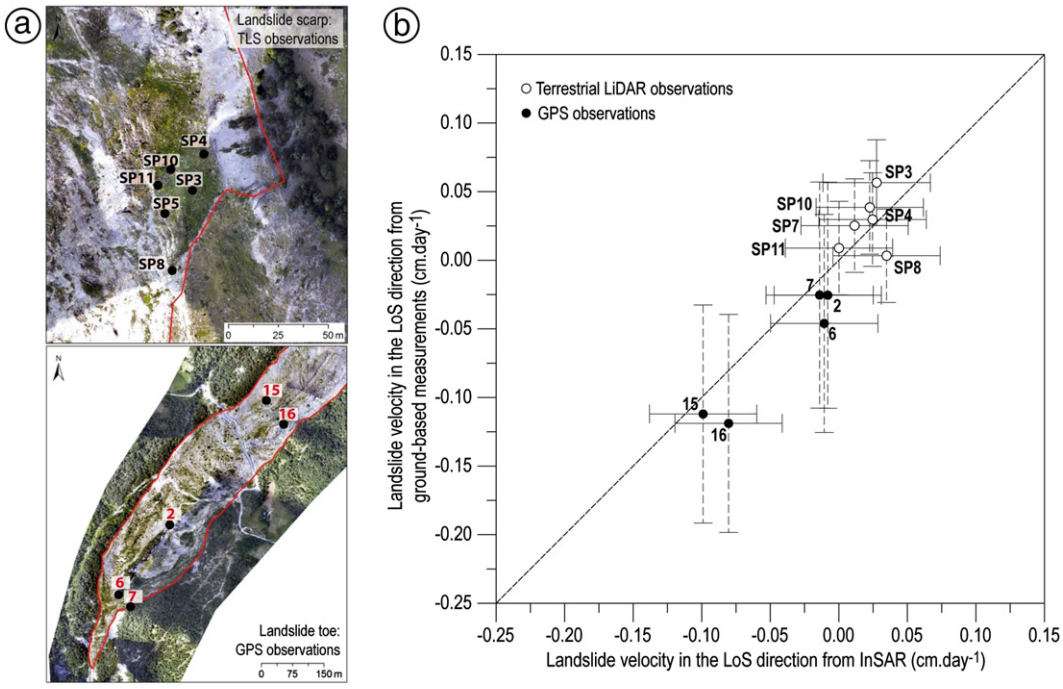

Fig. 8. Landslide velocity (vertical component and LoS direction) measured by InSAR and ground-based techniques (terrestrial LiDAR in the ablation zone and GPS in the accumulation zone) at La Valette for the period July–October 2009. The uncertainties of each measurement techniques are ±0.9 cm for InSAR, ±7 cm for GNSS, and ±3 cm for terrestrial LiDAR.

unwrapped using the branch-cut unwrapping algorithm of Goldstein et al. (1988). For case 4, unwrapping is not possible and only the wrapped phase is analysed.

3.2. Post-processing of the interferograms

All interferograms are co-registered and geocoded in cartographic coordinates (reference system Lambert 3) for comparison with other datasets. The analysis of landslide motion is then performed on small sub-scenes (2.1×1.9 km^2) of the interferograms around the two landslides (Fig. 5b).

The precise location and contours of the expected deformation area are mapped from a landslide inventory (1:3000) available for the whole region. The landslide morphological features (scarps, fractures, lobes, and gullies) observed on the aerial orthophotographs and the airborne LiDAR DSMs are used to guide the interpretation of the wrapped and unwrapped phase values.

In order to compare the interferograms, we shifted the phase values for the portions of the terrain out of the landslide limits. We subtracted the median phase values (Φ_{med}) of the area surrounding the landslide to the phase values of the sub-scene. The resulting phase values for the wrapped interferograms are thus expressed in the range $[-\pi\text{-}\Phi_{med}, \pi\text{-}\Phi_{med}]$. The shifted phase values are interpreted for zones of interest (200 m) around the landslides.

3.3. Interpretation of interferograms

To analyse the kinematics of the landslide (Fig. 6c), we convert the phase values (Φ) in displacement along the SAR LoS direction (D_{LoS}):

$$D_{LoS} = \lambda \Delta\Phi / 4\pi \quad (2)$$

where λ is the wavelength.

We further project the ground-based three-dimensional displacement vector U_G along the SAR LoS direction ($D_{G,\,LoS}$):

$$D_{G,\,LoS} = U_G . n_{LoS} \quad (3)$$

where n_{LoS} is the unit vector along the LoS direction, positively orientated in the satellite-ground direction. The n_{LoS} vector can be described in the East-North-Up reference system:

$$n_{LoS} = (\sin A_v \ \sin\theta, -\cos A_v \ \sin\theta, -\cos\theta) \quad (4)$$

where A_v is the mean azimuth of the LoS and θ is the incidence angle. In our case, the unit vector is defined with $n_{LoS} = [0.61, 0.15, -0.79]$, $A_v = 75.84°$ and $\theta = 38.7°$.

Taking into account the spatial distribution of the phase values, we consider the parts of the field with absolute phase values $\Phi > 0.5$ (corresponding to a displacement of 0.9 cm in LoS) as 'moving' areas (see Fig. 7 for the areas assumed to be stable in the regions of interest). As outlined in Fig. 1, various phase values and displacement fields can be observed at the scale of a landslide due to local movements:

- At the intermediate and lower parts of the landslides, the translational sliding movement can be mainly described by along-slope displacements: in a case of a small slope, as presented in Fig. 1, this movement corresponds to negative phase values ($\Phi < -0.5$). Moreover, the accumulation of the material in this part of the landslide eventually produces an upward movement of the ground, which increases the absolute phase value.
- In the upper part of the landslides, close to the main scarps, the vertical component of the displacement is dominant with a subsidence and a

Fig. 9. Displacement (cm) and velocity (cm day^{-1}) observed in the ablation zone of the Poche landslide from L-band PALSAR InSAR data. (a) Orthophotograph (2009) and interferograms for the periods T1, T2 and T3. (b) Profiles of elevation (top), D_{LoS} (middle) and D_{vert} (bottom) for two cross-sections perpendicular to the landslide (A–A′) and along the steepest slope direction (B–B′). The location of the two profiles (of width 30 m) is indicated in (a). The colour bars indicate changes in the size of different movement type (subsidence in red, transit in yellow to orange, and stable areas in green).

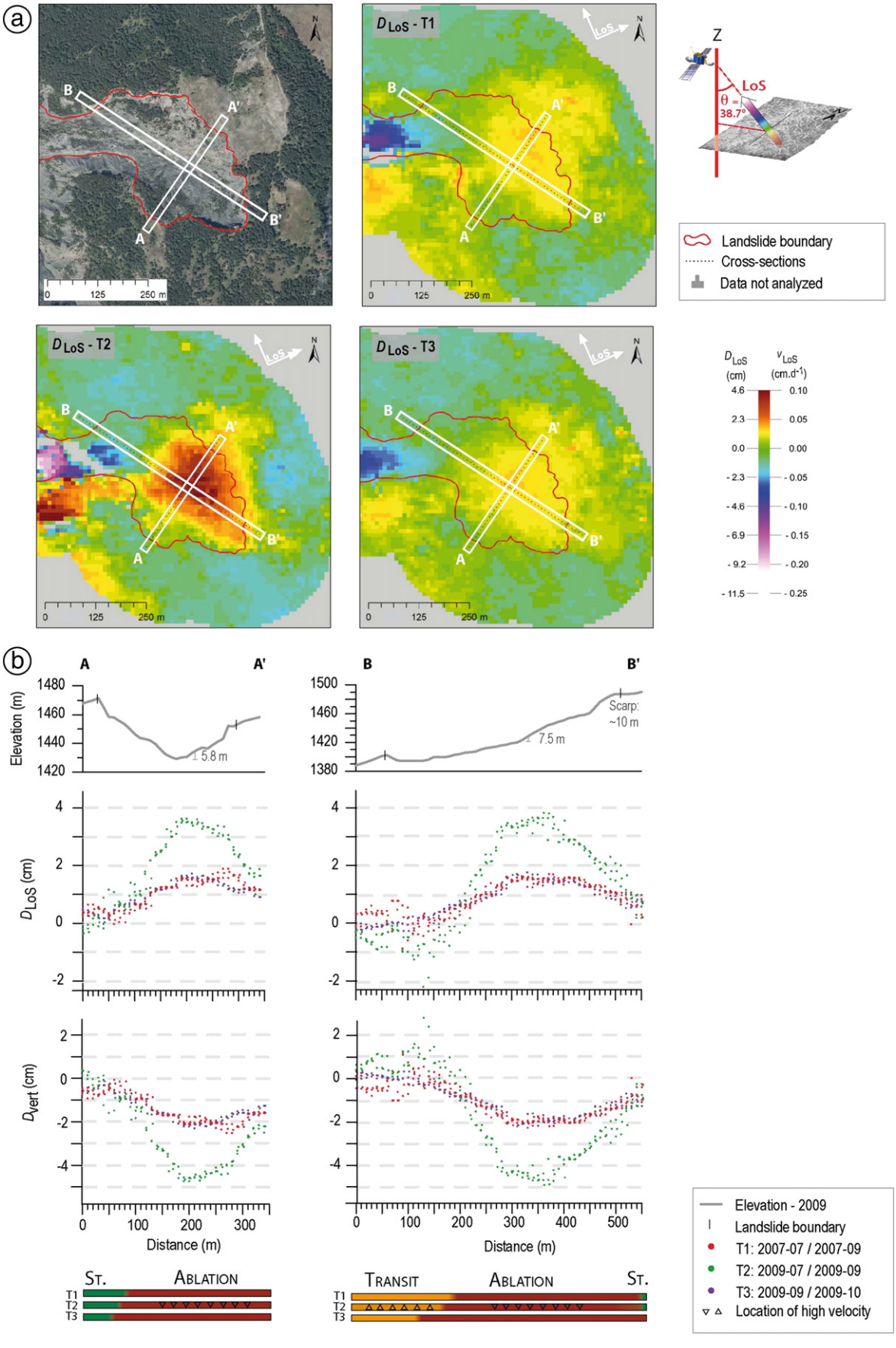
a
A
A'
B
B'
0 125 250 m
N
LoS
D LoS - T1
D LoS - T2
D LoS - T3
Z
LoS
θ = 38.7°
Landslide boundary
Cross-sections
Data not analyzed
D LoS (cm)
v LoS (cm.d-1)
4.6 0.10
2.3 0.05
0.0 0.00
- 2.3 - 0.05
- 4.6 - 0.10
- 6.9 - 0.15
- 9.2 - 0.20
- 11.5 - 0.25
b
Elevation (m)
1480
1460
1440
1420
5.8 m
1500
1460
1420
1380
Scarp: ~10 m
7.5 m
D LoS (cm)
D vert (cm)
Distance (m)
0 100 200 300
0 100 200 300 400 500
St. Ablation
Transit Ablation St.
T1
T2
T3
Elevation - 2009
Landslide boundary
T1: 2007-07 / 2007-09
T2: 2009-07 / 2009-09
T3: 2009-09 / 2009-10
Location of high velocity

loss of material; this movement corresponds to positive phase values ($\Phi > 0.5$).

If the displacements are large (e.g. higher than half the wavelength of the radar sensor), phase jumps can be observed due to the complexity of the unwrapping method. These SAR features, in relation with the morphological features, are interpreted either as a contact among a stable slope and the landslide, or as a contact among landslide units characterized by distinct displacement rates.

Using ground-based monitoring data, we assume a main displacement direction for all sub-units. Two cases are considered. The first case corresponds to a vertical motion associated with a depletion of material (preferentially located at the top of the landslide), or with an accumulation of material (preferentially at the toe of the landslide). Therefore, we convert the LoS displacement to ground vertical displacement (D_{vert}):

$$D_{vert} = D_{LoS}/(n_z.n_{LoS}) = -D_{LoS}/\cos\theta \quad (5)$$

where n_z is the vertical unit vector (positive upward).

A positive vertical displacement ($D_{vert} \geq 0$) corresponds to a subsidence; a negative vertical displacement ($D_{vert} \leq 0$) corresponds to an uplift.

The second case corresponds to an along-slope motion, observed for a translational sliding movement. We convert the LoS displacement to ground along-slope displacement (D_{Slope}):

$$D_{Slope} = D_{LoS}/\left(n_{Slope}.n_{LoS}\right) \quad (6)$$

where n_{Slope} is the unit vector (positive downslope) which can be written in the East-North-Up reference:

$$n_{Slope} = (\sin A_d \cos\alpha,\ \cos A_d \cos\alpha, -\sin\alpha) \quad (7)$$

where A_d is the slope azimuth angle, and α is the slope angle. For this analysis, A_d and α are calculated from a high (0.5 m) resolution LiDAR DSM available for the study area over a window of 9 × 9 pixels.

4. Data

The dataset consists of satellite SAR images, airborne orthophotographs, airborne laser scanning digital surface models (DSMs), and displacement measurements from ground-based GNSS or total stations. We use 15 ALOS/PALSAR images (processed at Level 1.0) acquired from March 2007 to July 2010 (Fig. 6). In C-band (λ = 5.6 cm) and X-band (λ = 3.1 cm) radar sensors, the phase quality of the SAR signal degrades due to changes in the backscattering properties of the ground surface (vegetation, soil surface state, micromorphology and roughness) which is less critical in L-band (λ = 23.8 cm) sensors (Rosen et al., 1996; Strozzi et al., 2005; Wei and Sandwell, 2010). For landslide monitoring, C-band images (ERS1/2) have been mainly used in the TANDEM acquisition mode with repeat cycle of 1–3 days (Rott et al., 1999; Squarzoni et al., 2003), while X-band sensors are only suitable for the monitoring of slopes with many natural reflectors (buildings and rocky blocks; Notti et al., 2010). Therefore, for the monitoring of large displacements, large wavelengths are more suitable (García-Davalillo et al., 2014).

The ALOS archive for the study area consists of images acquired in ascending orbit (track 880). Images acquired at the high resolution Fine Beam Polarization (FBS) mode are used. For all images, the pixel dimensions are 9.78 m in the azimuth direction and 7 m in the range direction; the mean look angle θ is 38.7° over the scene; and the off-nadir azimuth α_d is 75.84°. For the InSAR processing, the criteria used to select the image pairs are: (1) a perpendicular baseline ($B_\perp$) smaller than 1000 m; (2) a temporal baseline (B_T) between both images shorter than 92 days; and (3) a net rainfall amount of less than 220 mm between consecutive dates (Fig. 6). To avoid decorrelation due to the presence of snow cover, we also excluded scenes acquired in winter.

Table 3 details the dataset used for the analysis. A medium resolution (25 m) DSM from the French National Mapping Agency (BD ALTI®, IGN), resampled at 0.000088° (9.78 m) and projected in geographic-WGS84 coordinates was used for the InSAR processing. Very high resolution (0.5 m) airborne LiDAR DSMs and aerial orthophotographs (0.5 m) were used for the morphological and kinematic analysis of the landslides.

5. Results and discussion: quality of the processing and interpretation of landslide motion

The kinematics of the landslides was analysed for the period 2007–2010 in terms of both the spatial distribution of displacement rates and the evolution of rates over time. Four periods were considered: T1 = 2007-07-21 to 2007-09-05 (B_T = 46 days), T2 = 2009-07-26 to 2009-09-10 (46 days), T3 = 2009-09-10 to 2009-10-26 (46 days) and T4 = 2010-04-28 to 2010-07-29 (92 days).

Here we first discuss the quality of the InSAR results and then interpret the InSAR deformation field by taking into account geomorphological and geophysical knowledge of the landslides. The LoS displacements are interpreted in terms of vertical or along-slope displacements for landslide sub-units, and compared to ground-based geodetic observations. The landslide motion is then interpreted for the complete monitoring period. The results are discussed successively for each study case.

5.1. Quality and uncertainty of the InSAR phase values and deformation

A collocation error of 1.5 pixels (e.g. ca. 15 m) in the North and East components is observed on the SAR amplitude images and is taken into account for interpreting the LoS displacements. Even with interferograms at B_T = 46 days and $B_\perp < 1000$ m, decorrelation is observed because of important changes of the soil surface state (variation in soil humidity, transport of sediment, fracturing) especially in the ablation zones of the two landslides. For the Poche landslide, the unwrapped interferograms T1, T2 and T3 are considered of good quality because more than 95% of the phase values are unwrapped. The interferogram T4 (B_T = 92 days) cannot be interpreted because the coherence is too low over the area of interest. For the La Valette landslide, the interferograms have generally a lower quality (especially in the ablation zone); consequently, the phase values for T2, T3 and T4 cannot be unwrapped and only wrapped interferograms are used for the analysis.

The uncertainty of the phase values is estimated in terms of variability of the phase values on stable terrains outside of the landslides. For the four interferograms and the two landslides, more than 70% of pixels have a phase value in the range [−0.5 rad, +0.5 rad] (Fig. 7), except for Poche at T4. Atmospheric effects remain in the phase map, mainly for the La Valette landslide partly because of the large elevation range [1200–2200 m] (Fig. 7b).

Further, at La Valette, the InSAR velocity along the LoS direction is compared to projected ground-based velocity measured for 11 benchmarks (Travelletti et al., 2009, 2013). The results are presented in Fig. 8. The InSAR velocity is consistent with the ground-based observations with maximum errors of 0.05 cm day^{-1}.

5.2. Interpretation of the InSAR slope deformation field

Figs. 9 to 12 present the interferograms. The grey colour indicates areas where the phase values are not interpreted because of low coherence values (<0.3). In the following, the InSAR displacement field is interpreted successively for each case study.

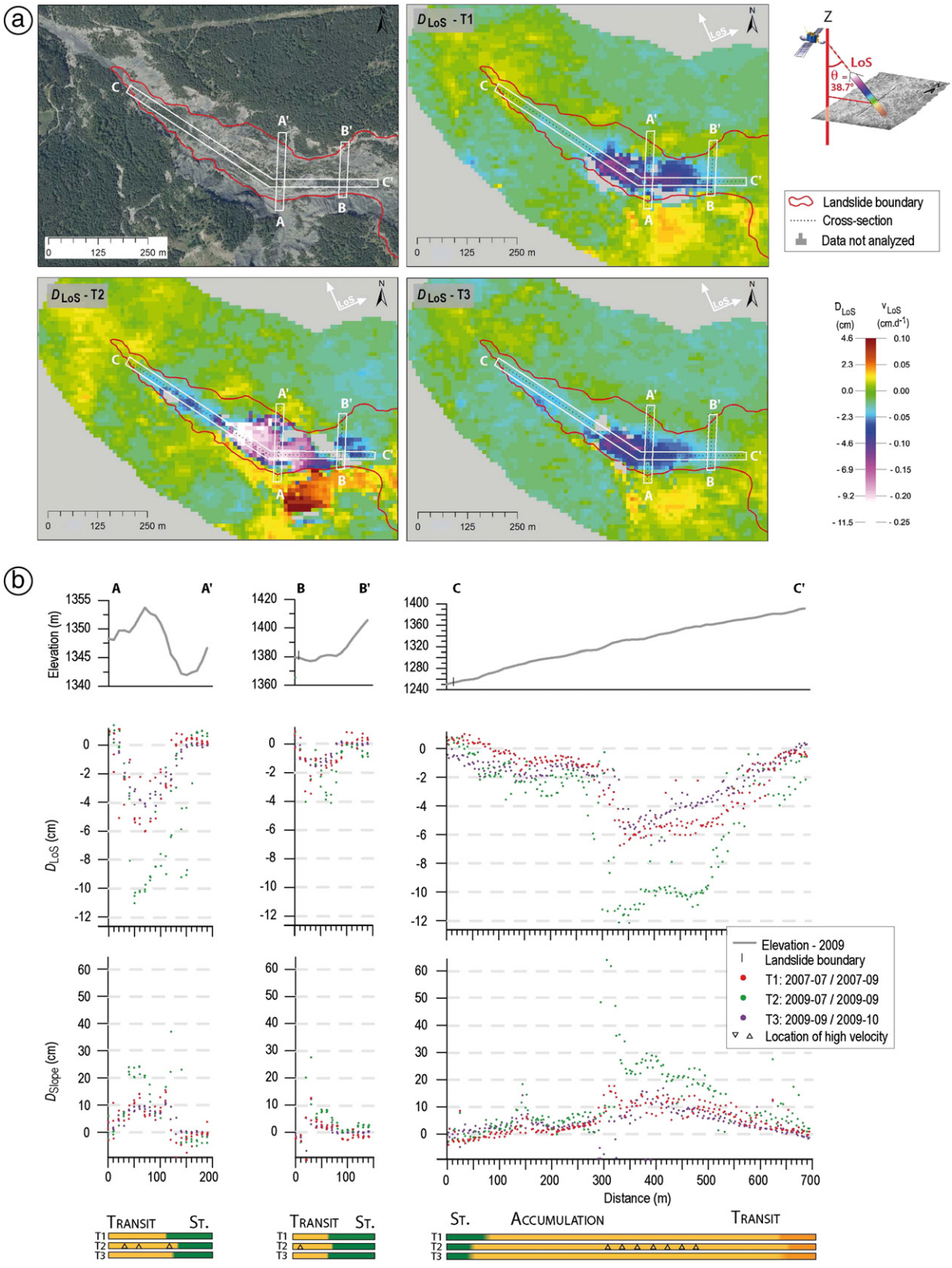

Fig. 10. Displacement (cm) and velocity (cm day^{-1}) observed in the transit-accumulation zone of the Poche landslide from L-band PALSAR InSAR data. (a) Orthophotograph (2009) and interferograms for the periods T1, T2 and T3. (b) Profiles of elevation (top), D_{LoS} (middle) and D_{slope} (bottom) for two cross-sections perpendicular to the steepest slope direction of the landslide (A–A′ and B–B′) and a cross-section along the steepest slope direction (C–C′). The location of the two profiles (of width 30 m) is indicated in (a). The colour bars indicate changes in the size of the movement type (subsidence in red, transit in yellow to orange, and stable slopes in green).

5.2.1. Case 1: InSAR deformation of the Poche ablation zone

In the ablation zone of the Poche landslide, we observe positive D_{LoS} values on the interferograms T1, T2 and T3 corresponding to a ground LoS displacement away from the satellite (Fig. 9a). A similar pattern is identified in the three interferograms. Morphological features (Figs. 1a and 3) and previous studies indicate a single rotational movement type (Le Mignon and Cojean, 2002).

For the three time periods, the subsidence is constrained within a circular area (diameter of ~300 m) with decreasing displacement rates from the centre to the edges (Fig. 9b). The amplitude of the displacement varies in time. The maximum absolute D_{LoS} values reach respectively ~2.1 ± 0.9 cm for T1, 3.8 ± 0.9 cm for T2 and 1.8 ± 0.9 cm for T3, corresponding to vertical displacements of ~2.7 ± 1.1, ~4.9 ± 1.1 and ~2.3 ± 1.1 cm, respectively. The spatial extent of the subsidence movement (e.g. $D_{LoS} \geq 0.9$ cm) is also different for the three periods (~11.2×10^4 m^2 for T1; ~9.2×10^4 m^2 for T2; and ~12.0×10^4 m^2 for T3). These observations indicate that the behaviour of the landslide is not steady-state with important changes in velocity over time.

To the South, the boundary of the subsidence corresponds to the previously mapped landslide morphological limits of 2009. To the Northeast, the subsidence signal extends far beyond the known landslide morphological limits (150 m away from the main scarp in the North-East direction; Fig. 9a) indicating a further extension of the landslide.

Two profiles clearly indicate the same deformation pattern with local sharp gradients corresponding to landslide morphological features or steep topography (Fig. 9b; A–A′, B–B′). Along the cross-section A–A′, the maximum subsidence rate occurs in the central part of a topographic depression, whereas convex slopes (e.g. secondary scarps) delimit the extension of the subsidence along the cross-section B–B′. In addition, positive centimetric D_{vert} values are observed for T2 on cross-section B–B′ (at abscissa 100 m) indicating accumulation of material, mainly to the West (Fig. 9b).

5.2.2. Case 2: InSAR deformation of the Poche transit-accumulation zone

In the transit-accumulation zone of the Poche landslide, we observe negative D_{LoS} values on the three interferograms T1, T2 and T3 corresponding to a ground LoS displacement towards the satellite (Fig. 10a). Taking into account both the azimuth and the slope of the landslide, we interpreted this movement as a translation movement type (Le Mignon and Cojean, 2002; Fig. 1b).

For the three time periods, the deformation is constrained within an ellipse (major axis length of 300 to 600 m) elongated in the E–W direction. The displacement rates are higher in the central part of the landslide, and decrease to the edges. The maximum deformation is observed close to a knick point where the sliding direction changes from N270° to N305°. Similar to the ablation zone, the amplitude of the displacement varies in time. The maximum absolute D_{LoS} values reach respectively 6.8 ± 0.9 cm for T1, 12.1 ± 0.9 cm for T2 and 6.4 ± 0.9 cm for T3, corresponding to D_{slope} values of ~18 ± 2.4, ~30 ± 2.2 and ~17 ± 2.4 cm, respectively. The spatial extent of the translational sliding (e.g. $D_{LoS} \geq 0.9$ cm in absolute values) is different for the three periods (~4.3×10^4 m^2 for T1; ~5.4×10^4 m^2 for T2; and ~5.0×10^4 m^2 for T3).

To the South and Southwest, the boundary of this deformation signal coincides with the steep scarp of the Poche torrent. To the South-East, a subsidence movement, associated with positive D_{LoS} values, corresponds to the progressive development of a shallow slump. On the contrary, no further extension of the landslide is observed to the North.

Three profiles clearly indicate the same deformation pattern with the succession of material accumulation in convex slopes and material erosion in concave slopes (Fig. 10b; A–A′, B–B′, C–C′). The spatial distribution of displacement rates suggests the occurrence of compression (convex slopes) and dilatation (concave slopes) according to the bedrock geometry.

5.2.3. Case 3: InSAR deformation of the La Valette transit-accumulation zone

Phase unwrapping is difficult for this case study because of higher displacement rates than for the Poche landslide and the related change of ground. Taking into account our criteria of analysis, the spatial extent of the zones with reliable phase values are respectively 3%, 18%, 13% and 38% for the periods T1, T2, T3 and T4 (Fig. 11a). The deformation pattern is however clearly depicted from the InSAR dataset. Similar to the case 2, the transit-accumulation zone of the La Valette landslide is characterized by negative D_{LoS} values on the interferograms T1, T2, T3 and T4 (Fig. 11a) corresponding to a ground LoS displacement towards the satellite (Fig. 11b). This movement is interpreted as a translation movement type (Hibert et al., 2012; Fig. 1b).

The maximum absolute D_{LoS} values reach respectively 8.9 ± 0.9 cm for T1, 14.7 ± 0.9 cm for T2 and 14.1 ± 0.9 cm for T3. For the three time periods, the deformation pattern has a clear flow-like shape (with a main sliding direction to the Southwest). The maximum deformation is located at the South, between the elevations 1650–1750 m, corresponding to a sharp gradient in the local topography. For the period T1, the InSAR depicts accumulation of material in the upper part of the transit zone (NW) and subsidence to the NE at the Rocher Blanc outcrop (Fig. 4b). For all periods, a decrease in displacement rates is observed from uphill to downhill; the distribution of displacement rates along the transverse cross-sections A–A′ and B–B′ suggests a laminar flow with higher velocity in the central part, and lower velocity along the edges.

5.2.4. Case 4: InSAR deformation of the La Valette ablation zone

The series of counterslopes, secondary scarps and grabens suggest that the type of movement consists of multiple rotational slides (Squarzoni et al., 2003; Travelletti et al., 2013; Fig. 1c). Numerous phase jumps are observed in the wrapped interferograms (Fig. 12a) especially for T3 and T4.

For the four time periods, the deformation is broadly constrained within the geomorphological boundaries of the landslide though some local enlargements are identified. To the SW, a new landslide tongue is progressively developing; to the East and Southeast, retrogression of the main scarp and a subsidence are observed.

The cross-sections A–A′ and B–B′, which show a large dispersion particularly along the section A–A′, indicate the same deformation pattern (Fig. 12b). The D_{LoS} values vary spatially along the landslide body confirming the complexity of the sliding motion. Changes in D_{LoS} trends are analysed along the cross-section A–A′ and B–B′ in order to map sub-units with different kinematics (Fig. 12b). Four sub-units, limited by morphological features, are identified from the wrapped phase values and are consistent with a graben structure.

5.3. Interpretation of landslide motion

The objective of this sub-section is to interpret the spatial and temporal variations in the amplitudes of displacement for the two landslides in relation with possible triggering factors.

Fig. 11. Displacement (cm) and velocity (cm day^{-1}) observed in the transit-accumulation zone of the La Valette landslide from L-band PALSAR InSAR data. (a) Orthophotograph (2009) and interferograms for the periods T1, T2, T3 and T4. The landslide boundary is represented in red. (b) Profiles of elevation (top), D_{LoS} (middle) and D_{vert} (bottom) for two cross-sections perpendicular to the landslide (A–A′ and B–B′) and a cross-section along the steepest slope direction (C–C′). The location of the two profiles (of width 30 m) is indicated in (a). The colour bars indicate changes in the size of the movement type (subsidence in red, transit in yellow to orange, and stable slopes in green).

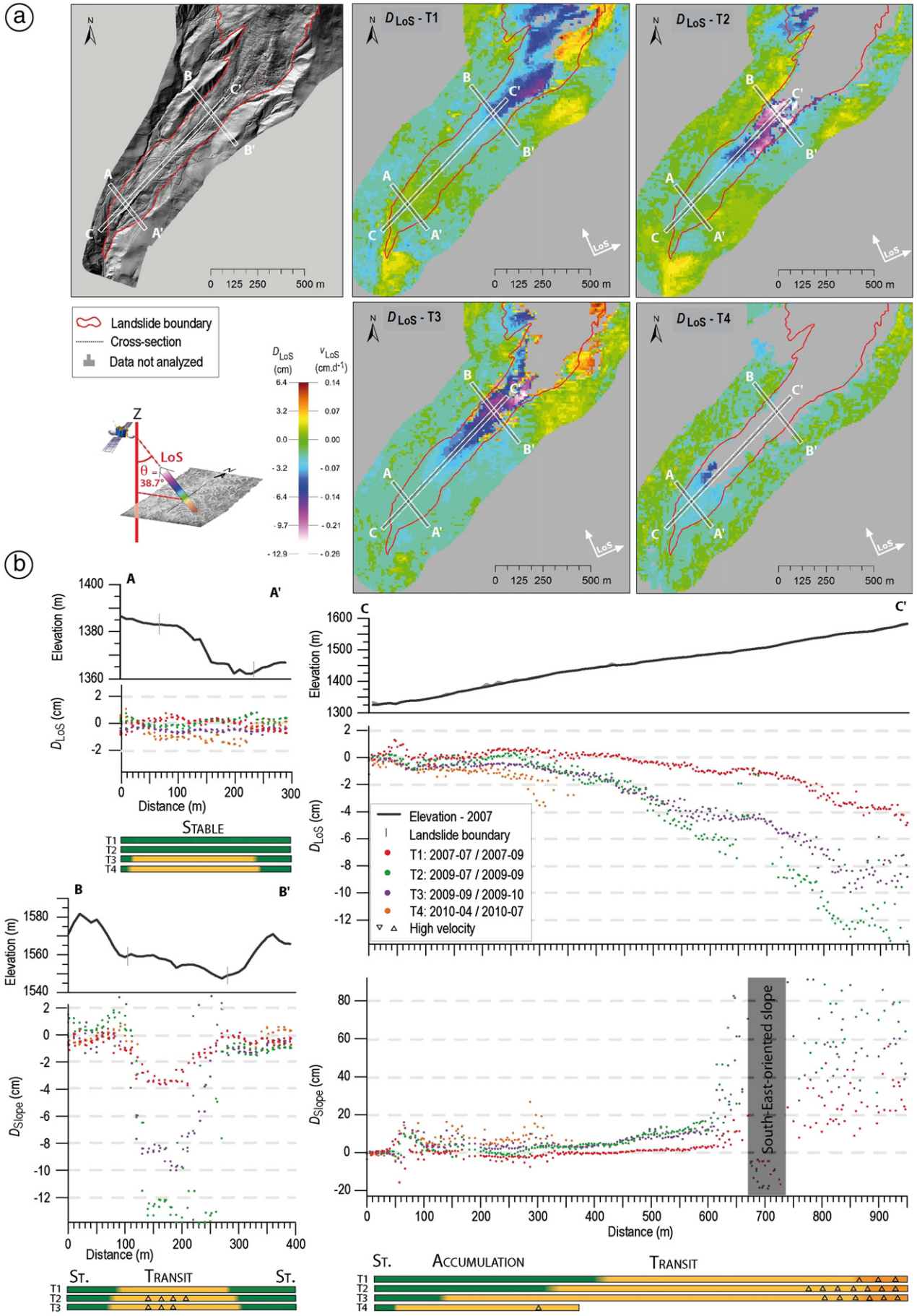
a
b
N
A
A'
B
B'
C
C'
0 125 250 500 m
D LoS - T1
D LoS - T2
D LoS - T3
D LoS - T4
LoS
Landslide boundary
Cross-section
Data not analyzed
D LoS (cm)
v LoS (cm.d-1)
6.4
3.2
0.0
-3.2
-6.4
-9.7
-12.9
0.14
0.07
0.00
-0.07
-0.14
-0.21
-0.28
Z
θ = 38.7°
Elevation (m)
D LoS (cm)
Distance (m)
STABLE
T1
T2
T3
T4
Elevation - 2007
Landslide boundary
T1: 2007-07 / 2007-09
T2: 2009-07 / 2009-09
T3: 2009-09 / 2009-10
T4: 2010-04 / 2010-07
High velocity
D Slope (cm)
South-East-oriented slope
ST.
TRANSIT
ACCUMULATION

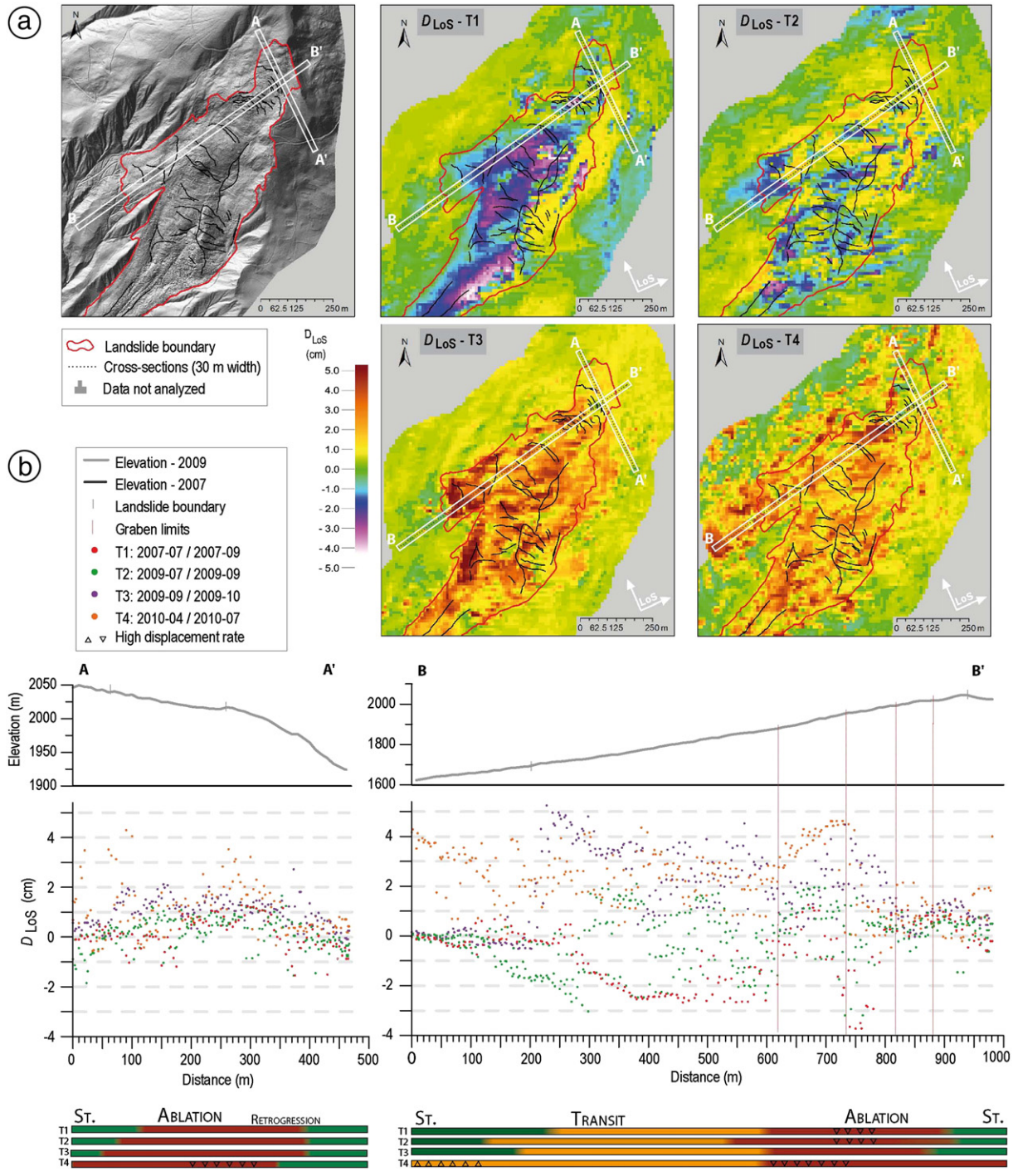

Fig. 12. Displacement (cm) and velocity (cm day^{-1}) observed in the ablation zone of the La Valette landslide from L-band PALSAR InSAR data. (a) Orthophotograph (2009) and interferograms for the periods T1, T2, T3 and T4. The landslide boundary is represented in red. (b) Profiles of elevation (top), D_{LoS} (middle) and D_{vert} (bottom) for two cross-section perpendicular to the landslide (A–A′) and along the steepest slope direction (B–B′). The location of the two profiles (of width 30 m) is indicated in (a). The colour bars indicate changes in the size of different movement type (subsidence in red, transit in yellow to orange, and stable slopes in green).

5.3.1. Kinematics of the Poche landslide

Fig. 13a shows the evolution of the D_{LoS} displacement rate of the Poche landslide for the periods T1, T2 and T3. In the ablation zone, the largest amplitudes of displacement are observed for T2 (summer 2009) and the lowest displacements are observed for T3 (autumn 2009). The subsidence rate is higher in summer 2009 (T2) than in summer 2007 (T1). At the opposite, in the transit zone, the displacements are in the same range for the three periods.

In comparison to the average velocity observed in the whole ablation and transit zones, a possible relation is observed between the surface velocity and the slope angle. The parts of the landslide with the highest velocity correspond to slopes around 20° for the ablation zone and 12° for the transit zone (Fig. 13b). The high displacement rates observed to the North and East of the ablation zone are confirmed by field observations which evidenced a retrogression of the main scarp between −3 and −9 m over the period 2007–2009. On-site EDM measurements on a

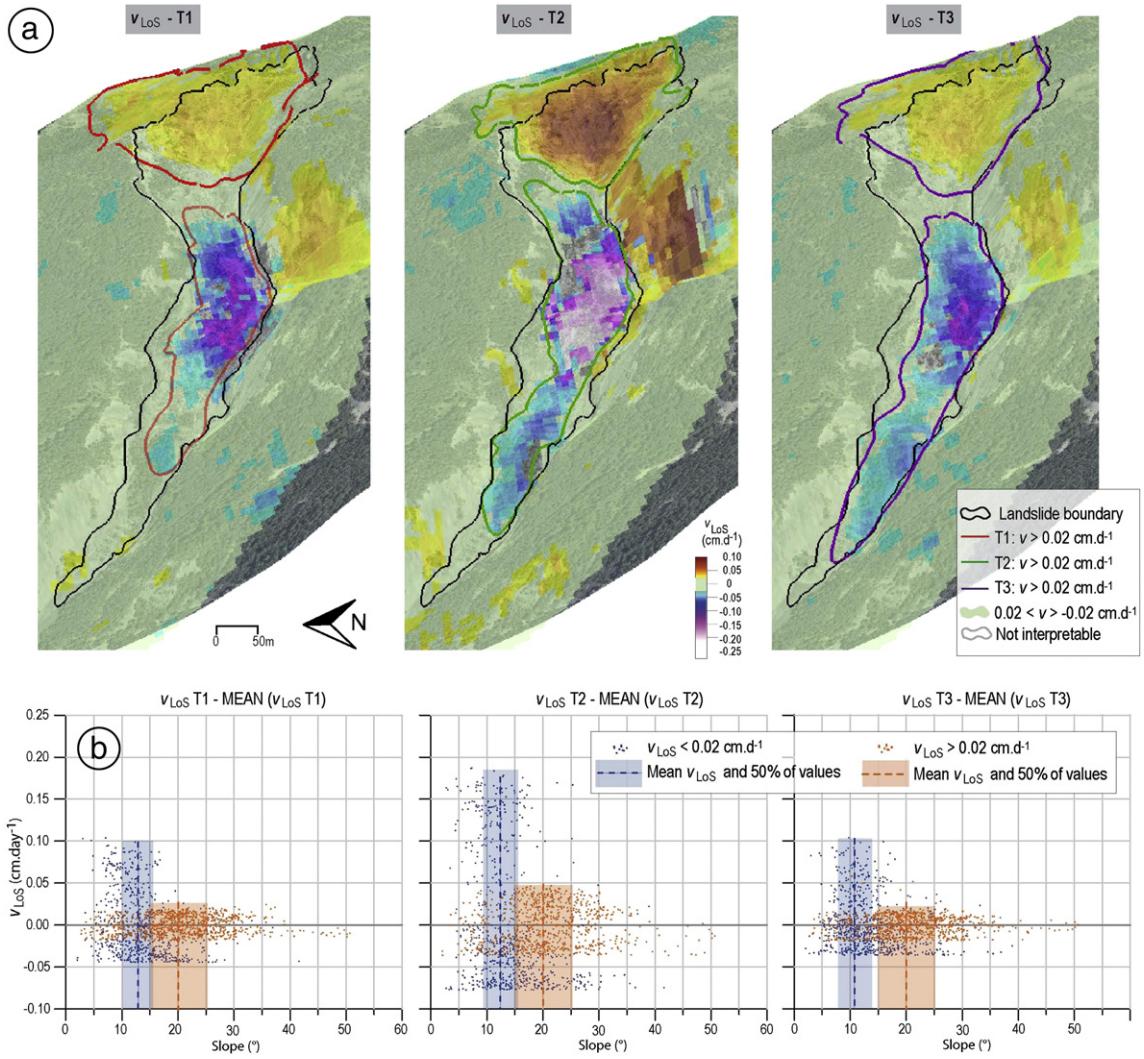

Fig. 13. InSAR displacement rates of the Poche landslide for three periods in 2007 and 2009. (a) Maps of v_{LoS} values (cm day^{-1}) at T1, T2 and T3. (b) Plots of v_{LoS} values as a function of slope angle (°). The velocity estimated at one pixel location is represented in relation to the average velocity observed in the subsidence zone ($v_{LoS} > 0.02$ cm d^{-1}, in orange) and in the transit zone ($v_{LoS} < 0.02$ cm d^{-1}, in blue).

series of benchmarks located along cross-section B–B′ (Fig. 9b) indicate an increase in the cumulative horizontal displacements from a total of 0.38 m in 2007 to a 0.60 m in 2009. Airborne orthophotographs for the same period show a similar pattern and amplitude of displacements. The highest displacement rates are observed at the point where the landslide changes its direction (from N270° to N300°) in relation with higher groundwater levels than at the terminal lobe.

5.3.2. Kinematics of the La Valette landslide

For the period 2007–2009, the evolution of the La Valette landslide (Fig. 14a) consists of a downslope progression of the main tongue and of a secondary tongue to the Northwest, of a retrogression of the main scarp and of a progressive increase of velocity in the lower parts.

The highest velocity (>0.02 cm day^{-1}) is observed in T2 (Fig. 15a). In comparison to the average velocity observed in the transit zones (Fig. 15b), the parts of the landslide with the highest velocity correspond to slope of around 17°. In the ablation zone, only wrapped phase values can be analysed. The retrogression and enlargement of the subsiding zone uphill occur at elevations higher than 1950 m. From the analysis of terrestrial LiDAR datasets for the period 2007–2009, Travelletti et al. (2013) estimate horizontal displacements of ca. 8 cm day^{-1} at 1950 m in elevation at the contact between the ablation and transit zones. Further downslope, the maximum D_{Slope} values estimated by InSAR decrease from 2 cm day^{-1} at 1600 m in elevation to 0.1 cm day^{-1} (T1) and 0.4 cm day^{-1} (T2, T3) at 1450 m in elevation, and further decrease towards the toe. Our results are consistent with the previous studies even considering different observation periods.

With C-band ERS images, Squarzoni et al. (2005) estimate displacement rates in the same order of magnitude than our results, and comprised between ~0.5 cm day^{-1} in 1999 to ~2 cm day^{-1} in 1996. With X-band TerraSAR-X images, Raucoules et al. (2013) are able to map the 3D landslide deformation pattern for the period 2010–2011 using amplitude offsets. They estimate maximum rates in the order of $D_{horiz} \approx 3.8$ cm day^{-1} and $D_{vert} \approx 3$ cm day^{-1} in the ablation area, which are higher than the displacements estimated for 2007 and 2009. They also notice the highest displacement rates in the months April to July (e.g. with velocity up to 5.5 cm day^{-1}). The same temporal pattern is observed in our dataset for the year 2009, with higher velocities in late spring/early summer than in autumn.

5.3.3. Triggering factors

For the two landslides, higher displacement rates are observed for the periods T2 and T4 in relation with larger amounts of net and effective (precipitation minus evapotranspiration) cumulated rainfall over 120 days (Fig. 15a). The evapotranspiration rate is calculated with the Penman–Monteith method. The effective cumulative rainfalls for the 30 days before the first SAR image acquisition are higher for T2

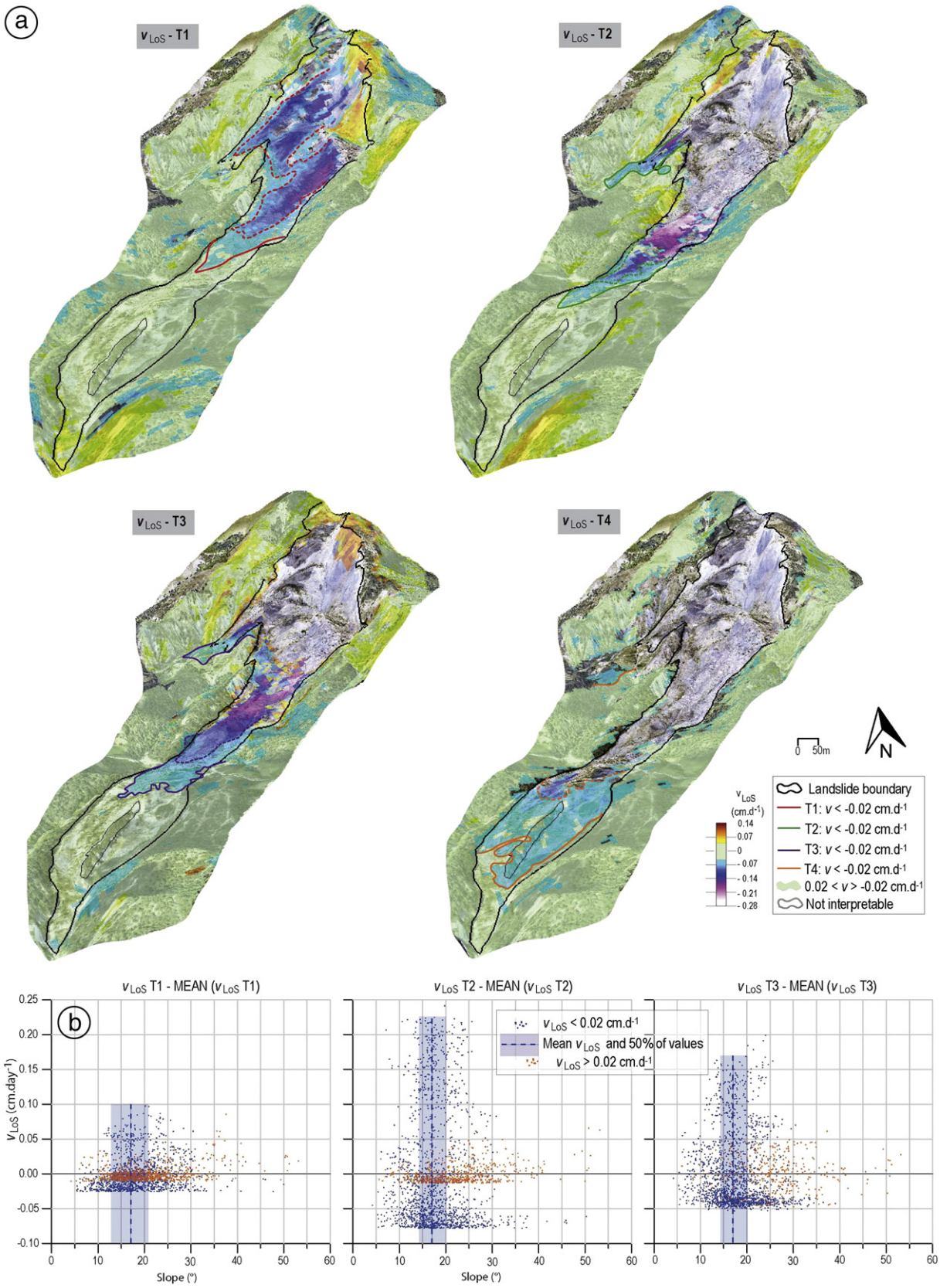

Fig. 14. InSAR displacement rates of the La Valette landslide for three periods in 2007 and 2009. (a) Maps of v_{LoS} values (cm day^{-1}) at T1, T2, T3 and T4; (b) plots of v_{LoS} values as a function of slope angle (°). The velocity estimated at one pixel location is represented in relation to the average velocity observed in the subsidence zone (v_{LoS} > 0.02 cm d^{-1}, in orange) and in the transit zone (v_{LoS} < 0.02 cm d^{-1}, in blue).

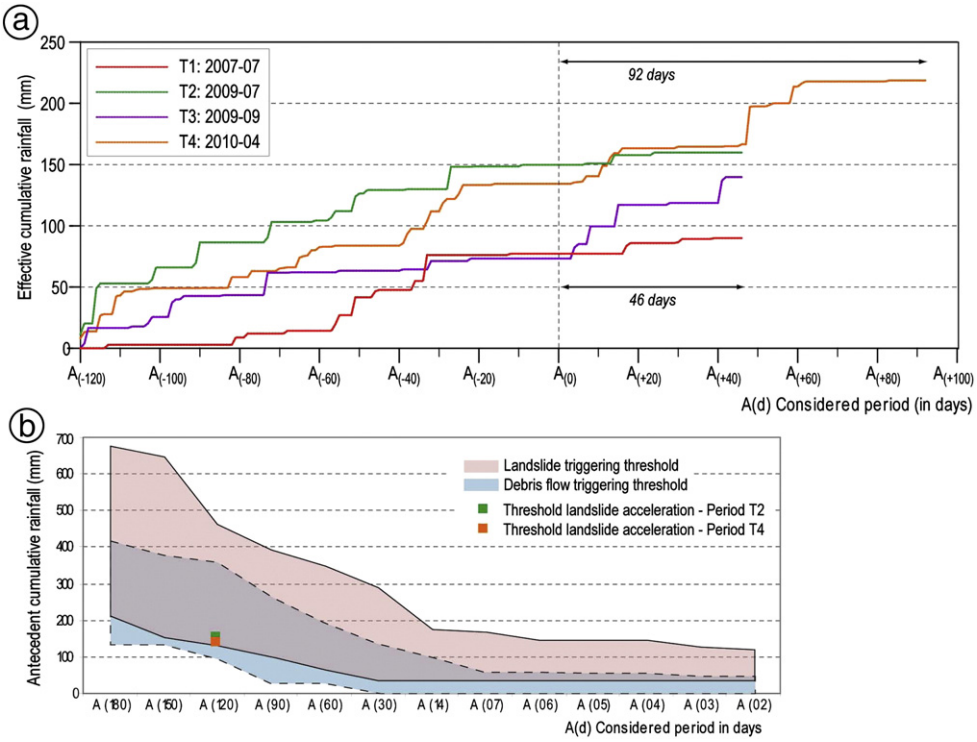

Fig. 15. Effect of rainfall amount on landslide motion. Cumulative effective rainfall observed before and during the four InSAR monitoring periods T1 to T4. The rainfall amounts are sampled at the Barcelonnette meteorological station; (b) landslide triggering rainfall thresholds estimated for the Barcelonnette region and threshold for landslide acceleration identified for two InSAR monitoring periods (T2, T4).

(20 mm) and T4 (22.5 mm) than for T1 (1.0 mm) and T3 (2.0 mm). These rainfall amounts (corresponding to landslide acceleration) are consistent with the antecedent cumulative rainfall thresholds proposed by Remaître and Malet (submitted for publication) from the analysis of the triggering conditions of 150 dated landslide and debris flow events in the Barcelonnette Basin over the period 1920–2010 (Fig. 15b).

6. Conclusion

This work demonstrates the potential of L-band ALOS/PALSAR archive images to analyse the deformation pattern of large and rapid landslides. For such case studies, the longer wavelength of L-band SAR sensors are suitable to preserve high spatial and temporal correlations and to cover vegetated landslides or ground affected by important soil surface changes. In order to overcome some limitations of InSAR processing in complex mountainous terrains, the different contributions to the SAR interferometric phase are estimated: the topography and the atmospheric delay are corrected, and a power spectrum filtering is applied on each interferogram.

A geomorphological-guided interpretation method is proposed to interpret the wrapped or unwrapped phase values for the location where the coherence value is higher than 0.3. The method integrates information on the location of specific morphological (scarps, grabens, and lobes) or topographic (steep slopes and convexity–concavity) features to analyse the spatial distribution of phase values. An *a priori* knowledge on the landslide deformation pattern (morphology and ground-based surface displacement monitoring) is used to convert and project the phase values into ground displacement. The processing is finely tuned for case studies corresponding to rotational movement, translational movement or complex movement and for two ranges of displacement rates (≤ 0.4 and >0.4 cm day^{-1}).

The results indicate that the deformation of two landslides can be monitored with ALOS/PALSAR imagery even with limited available SAR data. However, a larger and complete set of data would allow us to monitor the landslide evolution over several years using time series analysis and then estimate the relationships with the meteorological controlling factors with higher accuracy. The estimated displacement rates are in the range of the ground-based observations (GNSS and EDM) and consistent with C-band and X-band InSAR displacement rates estimated for other time periods. Highly variable displacement in space and time is identified for the two landslides in relation with rainfalls; enlargements and retrogression of the landslides scarps are also detectable for both landslides.

The proposed interpretation method is of interest for both 1) the detection and mapping of landslides in mountainous and vegetated terrains, and 2) the analysis of landslide mechanisms. ALOS/PALSAR imagery, even if only limited archive data are available, allows complementing information from other satellite SAR sensors to construct long time series of surface deformation. Further developments are the use of the spatial distribution of the deformation to infer the geometry and volume of the displaced material, and to characterize the rheology of the moving mass.

Acknowledgements

This work has been supported by the Marie Curie Research and Initial Training Network "CHANGES: Changing Hydro-meteorological Risks as Analyzed by a New Generation of European Scientists", funded by the European Community's 7th Framework Programme FP7/2007–2013 under Grant Agreement No. 263953. ALOS/PALSAR images were provided by the Japan Aerospace Exploration Agency (JAXA) and the European Space Agency (ESA) under the contract C1P.8859. The GNSS data were provided by the French Landslide Observatory (OMIV: Observatoire Multidisciplinaire des Instabilités de Versants: http://omiv.unistra.fr). The EDM measurements were acquired by the RTM-04 (Restauration des Terrains en Montagne) service of Département des Alpes-de-Haute-Provence.

References

Bardi, F., Frodella, W., Ciampalini, A., Bianchini, S., Del Ventisette, C., Gigli, G., Fanti, R., Moretti, S., Basile, G., Casagli, N., 2014. Integration between ground based and satellite SAR data in landslide mapping: the San Fratello case study. Geomorphology 223, 45–60.

Beauducel, F., Briole, P., 2000. Volcano-wide fringes in ERS synthetic aperture radar interferograms of Etna (1992–1998): deformation or tropospheric effect? J. Geophys. Res. 105 (B7), 16391–16402.

Berardino, P., Fornaro, G., Lanari, R., Sansosti, E., 2002. A new algorithm for surface deformation monitoring based on small baseline differential SAR interferograms. IEEE Trans. Geosci. Remote Sens. 40 (11), 2375–2383.

Booth, A.M., Lamb, M.P., Avouac, J.-P., Delacourt, C., 2013. Landslide velocity, thickness, and rheology from remote sensing: La Clapière landslide, France. Geophys. Res. Lett. 40, 4299–4304.

Cascini, L., Fornaro, G., Peduto, D., 2009. Analysis at medium scale of low-resolution DInSAR data in slow-moving landslide-affected areas. ISPRS J. Photogramm. Remote Sens. 64, 598–611.

Catani, F., Farina, P., Moretti, S., Nico, G., Strozzi, T., 2005. On the application of SAR interferometry to geomorphological studies: estimation of landform attributes and mass movements. Geomorphology 66, 119–131.

Cruden, D.M., Varnes, D.J., 1996. Landslide types and processes. In: Turner, R.L., Schuster, A.K. (Eds.), Landslide Investigations and Mitigation. Transportation Research Board, Washington D.C., pp. 36–75.

Delacourt, C., Allemand, P., Berthier, E., Raucoules, D., Casson, B., Grandjean, P., Pambrun, C., Varel, E., 2007. Remote-sensing techniques for analysing landslide kinematics: a review. Bull. Soc. Geol. Fr. 178, 89–100.

Dikau, R., Brunsden, D., Schrott, L., Ibsen, M.-L., 1996. Landslide Recognition: Identification, Movement and Causes. Wiley, Chichester.

Doin, M.P., Lasserre, C., Peltzer, G., Cavalie, O., 2009. Corrections of stratified tropospheric delays in SAR interferometry: validation with global atmospheric models. J. Appl. Geophys. 69, 35–50.

Doin, M., Lodge, F., Guillaso, S., Jolivet, R., Lasserre, C., Ducret, G., Grandin, R., Pathier, E., Pinel, V., 2011. Presentation of the small baseline processing chain on a case example: the Etna deformation monitoring from 2003 to 2010 using ENVISAT data. Proceeding Fringe 2011, ESA, Frascati, Italy, 19–23 September 2011, pp. 1–7.

Farina, P., Colombo, D., Fumagalli, A., Marks, F., Moretti, S., 2006. Permanent scatterers for landslide investigations: outcomes from the ESA-SLAM project. Eng. Geol. 88, 200–217.

Ferretti, A., Prati, C., Rocca, C., 2001. Permanent scatterers in SAR interferometry. IEEE Trans. Geosci. Remote Sens. 39 (1), 8–20.

García-Davalillo, J.-C., Herrera, G., Notti, D., Strozzi, T., Álvarez-Fernández, I., 2014. DInSAR analysis of ALOS PALSAR images for the assessment of very slow landslides: the Tena Valley case study. Landslides 11, 225–246.

Goldstein, R.M.M., Zebker, H.A., Werner, C.L., 1988. Satellite radar interferometry: two-dimensional phase unwrapping. Radio Sci. 23, 713–720.

Guzzetti, F., Manunta, M., Ardizzone, F., Pepe, A., Cardinali, M., Zeni, G., Reichenbach, P., Lanari, R., 2009. Analysis of ground deformation detected using the SBAS-DInSAR technique in Umbria, Central Italy. Pure Appl. Geophys. 166, 1425–1459.

Guzzetti, F., Mondini, A.C., Cardinali, M., Fiorucci, F., Santangelo, M., Chang, K.-T., 2012. Landslide inventory maps: new tools for an old problem. Earth Sci. Rev. 112, 42–66.

Hibert, C., Grandjean, G., Bitri, A., Travelletti, J., Malet, J.-P., 2012. Characterizing landslides through geophysical data fusion: example of the La Valette landslide (France). Eng. Geol. 128, 23–29.

Hilley, G.E., Bu, R., Ferretti, A., Novali, F., Rocca, F., 2004. Dynamics of slow-moving landslides from permanent scatterer analysis. Science 304, 1952–1955.

Hooper, A., 2004. A new method for measuring deformation on volcanoes and other natural terrains using InSAR persistent scatterers. Geophys. Res. Lett. 31, L23611. http://dx.doi.org/10.1029/2004GL021737.

Jebur, M.N., Pradhan, B., Tehrany, M.S., 2014. Detection of vertical slope movement in highly vegetated tropical area of Gunung pass landslide, Malaysia, using L-band InSAR technique. Geosci. J. 18, 61–68.

Lauknes, T.R., Shanker, A.P., Dehls, J.F., Zebker, H.A., Henderson, I.H.C., Larsen, Y., 2010. Remote sensing of environment detailed rockslide mapping in northern Norway with small baseline and persistent scatterer interferometric SAR time series methods. Remote Sens. Environ. 114, 2097–2109.

Le Mignon, G., Cojean, R., 2002. Rôle de l'eau dans la remobilisation de glissements–coulées (Barcelonnette, France). In: Rybar, J., Stemberk, J., Wagner, P. (Eds.), Proceedings of the 1st European Conference on Landslides, Prague, Czech Republik, Swets & Zeiltinger, Lisse, pp. 239–244.

Leprince, S., Berthier, E., Ayoub, F., Delacourt, C., Avouac, J.-P., 2008. Monitoring earth surface dynamics with optical imagery. Eos 89, 1–4.

Malet, J.-P., Maquaire, O., 2003. Black marl earthflows mobility and long-term seasonal dynamic in southeastern France. In: Picarelli, L. (Ed.), Fast Slope Movements: Prediction and Prevention for Risk Mitigation. Patron Editore, Bologna, pp. 333–340.

Malet, J.-P., Maquaire, O., Calais, E., 2002. The use of Global Positioning System techniques for the continuous monitoring of landslides: application to the Super-Sauze earthflow (Alpes-de-Haute-Provence, France). Geomorphology 43, 33–54.

Malet, J.P., Ulrich, P., Déprez, A., Masson, F., Lissak, C., Maquaire, O., 2013. Continuous monitoring and near-real time processing of GPS observations for landslide analysis: a methodological framework. In: Margottini, C., Canuti, P. Sassa (Eds.), Landslide Science and Practice. Proceedings of the Second World Landslide Forum Vol. 2. Springer, Rome, Italy, pp. 201–209. http://dx.doi.org/10.1007/978-3-642-31445-2_26.

Massonnet, D., Feigl, K.L., 1998. Radar interferometry and its application to changes in the Earth's surface. Rev. Geophys. 36, 441–500.

Muller, J.R., Martel, S.J., 2000. Numerical models of translational landslide rupture surface growth. Pure Appl. Geophys. 157, 1009–1038.

Nikolaeva, E., Walter, T.R., Shirzaei, M., Zschau, J., 2014. Landslide observation and volume estimation in central Georgia based on L-band InSAR. Nat. Hazards Earth Syst. Sci. 14, 675–688.

Notti, D., Davalillo, J.C., Herrera, G., Mora, O., Ferrata, V., 2010. Assessment of the performance of X-band satellite radar data for landslide mapping and monitoring: upper Tena Valley case study. Nat. Hazards Earth Syst. Sci. 10, 1865–1875.

Okada, Y., 1985. Surface deformation due to shear and tensile faults in a half-space. Int. J. Rock Mech. Min. Sci. Geomech. Abstr. 75, 1135–1154.

Petley, D.N., Bulmer, M.H., Murphy, W., 2002. Patterns of movement in rotational and translational landslides. Geology 30, 719–722.

Raucoules, D., De Michele, M., Malet, J., Ulrich, P., 2013. Remote sensing of environment time-variable 3D ground displacements from high-resolution synthetic aperture radar (SAR). Application to La Valette landslide (South French Alps). Remote Sens. Environ. 139, 198–204.

Remaître, A., Malet, J.-P., 2014. Rainfall patterns and climatic conditions associated to the triggering of fast- and slow-moving landslides at different time scales. A case study in the South French Alps. Landslides (submitted for publication).

Rosen, P.A., Hensley, S., Zebker, H.A., Webb, F.H., Fielding, E.J., 1996. Surface deformation and coherence measurements of Kilauea Volcano, Hawaii, from SIR-C radar interferometry. J. Geophys. Res. 101 (E10), 23109–23125.

Rosen, P.A., Hensley, S., Peltzer, G., Simons, M., 2004. Updated repeat orbit interferometry package released. EOS Trans. Am. Geophys. Union 85, 47–48.

Rott, H., Scheuchl, B., Siegel, A., 1999. Monitoring very slow slope movements by means of SAR interferometry: a case study from a mass waste above a reservoir in the Ötztal Alps, Austria. Geophys. Res. Lett. 26, 1629–1632.

Schmutz, M., 2000. Apport des méthodes géophysiques à la connaissance des glissements-coulées développés dans les marnes noires. (Thèse de doctorat). Application à Super Sauze (Alpes-de-Haute-Provence, France). Université Louis Pasteur, Strasbourg, France.

Squarzoni, C., Delacourt, C., Allemand, P., 2003. Nine years of spatial and temporal evolution of the La Valette landslide observed by SAR interferometry. Eng. Geol. 68, 53–66.

Squarzoni, C., Delacourt, C., Allemand, P., 2005. Differential single-frequency GPS monitoring of the La Valette landslide (French Alps). Eng. Geol. 79, 215–229.

Strozzi, T., Farina, P., Corsini, A., Ambrosi, C., Thüring, M., Zilger, J., Wiesmann, A., Wegmüller, U., Werner, C., 2005. Survey and monitoring of landslide displacements by means of L-band satellite SAR interferometry. Landslides 2, 193–201.

Stumpf, A., Malet, J.-P., Kerle, N., Niethammer, U., Rothmund, S., 2013. Image-based mapping of surface fissures for the investigation of landslide dynamics. Geomorphology 186, 12–27.

Stumpf, A., Malet, J.-P., Allemand, P., Ulrich, P., 2014. Surface reconstruction and landslide displacement measurements with Pléiades satellite images. ISPRS J. Photogramm. Remote Sens. 95, 1–12.

Tofani, V., Segoni, S., Agostini, A., Catani, F., Casagli, N., 2013. Use of remote sensing for landslide studies in Europe. Nat. Hazards Earth Syst. Sci. 13, 299–309.

Tolomei, C., Taramelli, A., Moro, M., Saroli, M., Aringoli, D., Salvi, S., 2013. Analysis of the deep-seated gravitational slope deformations over Mt. Frascare (Central Italy) with geomorphological assessment and DInSAR approaches. Geomorphology 201, 281–292.

Travelletti, J., Malet, J., Hibert, C., Grandjean, G., 2009. Integration of geomorphological, geophysical and geotechnical data to define the 3D morpho-structure of the La Valette mudslide, Ubaye Valley, French Alps. In: Malet, J.-P., Remaître, A., Boogard, T.A. (Eds.), Proceedings of the International Conference: Landslide Processes: From Geomorphologic Mapping to Dynamic Modelling. CERG Editions, Strasbourg, pp. 203–208.

Travelletti, J., Delacourt, C., Allemand, P., Malet, J.-P., Schmittbuhl, J., Toussaint, R., Bastard, M., 2012. Correlation of multi-temporal ground-based optical images for landslide monitoring: application, potential and limitations. ISPRS J. Photogramm. Remote Sens. 70, 39–55.

Travelletti, J., Malet, J.-P., Samyn, K., Grandjean, G., Jaboyedoff, M., 2013. Control of landslide retrogression by discontinuities: evidence by the integration of airborne- and ground-based geophysical information. Landslides 10, 37–54.

Vietmeier, J., Wagner, W., Dikau, R., 1999. Monitoring moderate slope movements (landslides) in the southern French Alps using differential SAR interferometry. Proc. 2nd International Workshop on ERS SAR Interferometry, FRINGE99, 10–12 November 1999. Liège, Belgium, pp. 31–40.

Wei, M., Sandwell, D.T., 2010. Decorrelation of L-Band and C-Band interferometry over vegetated areas in California. IEEE Trans. Geosci. Remote Sens. 48, 2942–2952.

Zhao, C., Lu, Z., Zhang, Q., De, J., 2012. Large-area landslide detection and monitoring with ALOS / PALSAR imagery data over Northern California and Southern Oregon, USA. Remote Sens. Environ. 124, 348–359.

Zhao, C., Zhang, Q., Yin, Y., Lu, Z., Yang, C., Zhu, W., Li, B., 2013. Pre-, co-, and post-rockslide analysis with ALOS/PALSAR imagery: a case study of the Jiweishan rockslide, China. Nat. Hazards Earth Syst. Sci. 13, 2851–2861.